RSC Advances

ROYAL SOCIETY OF CHEMISTRY

www.rsc.org/advances

Graphical Abstract

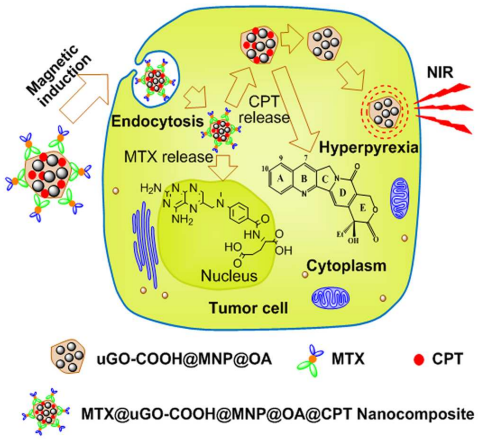

The graphene oxide/Fe_3O_4 nanocomposite against drug-resistant tumor by the combination of dual-drug chemotherapy and photothermal therapy with NIR.

Graphene oxide/Fe_3O_4 nanocomposite for combination of dual-drug chemotherapy with photothermal therapy

Jian-Min Shen[a*], Fei-Yun Gao[b], Li-Ping Guan[a], Wen Su[a], Yan-Jie Yang[c], Qian-Rong Li[a], Zhong-Cai Jin[a]

[a] Department of Biochemistry and Molecular Biology, School of Life Sciences, Lanzhou University, Lanzhou, Gansu 730000, China

[b] Key Lab of Preclinical Study for New Drugs of Gansu Province, Lanzhou, Gansu 730000, China

[c] College of Chemistry and Chemical Engineering, Lanzhou University, Lanzhou, Gansu 730000, China

[*] Corresponding author:Jian-Min Shen. Tel.: +86-15117266908; fax: +86-931-891-5208.
E-mail address: shenjianmin@lzu.edu.cn (Jianmin Shen)

Abstract:

Multi-modal strategies may enhance anticancer efficacy by overcoming tumor drug resistance due to different anticancer pathway and mechanism. Herein, a novel method of synthesizing ultra-fine graphene oxide (uGO)/magnetic nanoparticle (MNP) composite is presented. This composite is fabricated by combination of a simple and effective chemical deposition with further oxidation of iron ions on carboxylated uGO base, followed by coating oleic acid on MNPs. Two anticancer drugs, camptothecin (CPT) and methotrexate (MTX), are separately bound to uGO sheets and the carboxyl terminals of uGO on the hybrid, forming a superparamagnetic & dual drug-loaded MTX@uGO-COOH@MNP@OA@CPT nanocomposite. The size of the composite is approximately 80 nm by DLS. The entrapment efficiencies of MNPs, CPT, and MTX reach approximately 458 mg/g, 682 mg/g, and 896 mg/g, respectively. In vitro release and apoptotic assay results show that the nanocomposite can cause the apoptosis and death of HepG2 cells by preferential releasing drugs to tumor microenvironment. The tumor inhibitory rate of 73.9% in the S-180 sarcoma-bearing Balb/c mice suggests that the combination of nanocomposite-mediated dual drug synergic chemotherapy with photothermal therapy has remarkable therapeutic potential against drug-resistant tumors.

Keywords: Graphene oxide (GO); magnetic nanoparticles (MNPs); drug delivery system; chemotherapy; photothermal therapy

1. Introduction

A major obstacle to successful tumor chemotherapy is known to be cytotoxic drug resistance,[1] which has become a key issue in the current research of anticancer. DNA is one of the traditional targets of chemotherapy drugs.[2] The cell toxicity of these drugs is associated with tumor DNA damage. When DNA was damaged, however, the body can enhance DNA repair by quickly synthesizing endonuclease, DNA polymerase, and DNA ligase.[3] In addition, when the drug exposure occurs in the body, it is possible to activate the pathway of metabolism and detoxification of glutathione and related enzymes, in turn, perform the drug clearance.[4] Single administered drug therapy, furthermore, can produce compensatory materials for tumor growth by other pathways.[5,6] All of these above will cause drug resistance. Actually, combination of multi-drug therapy with site-directed drug targeting can not only effectively block the occurrence of repair, clearance, and compensation to a certain degree,[7] but also can reduce the dosage of drug and carrier, and decrease undesirable side effects.[8] According to the literatures, some anticancer agents can lead to the growth inhibition of rapidly dividing cells either by the stable combination with topoisomerase I and DNA, such as camptothecin (CPT),[9] or by the intercalative binding to DNA, such as methotrexate (MTX).[10] If a simultaneously administered therapy of CPT and MTX was achieved, it may enhance anticancer efficacy by alleviating drug resistance due to the different anticancer pathway.

Common polymer micelles, however, are unable to accommodate various drugs in the form of separation from each other. The drugs usually mix with each other in the matrix of carriers,[11,12] which affects the medicinal property of drugs and reduces the efficacy of co-therapy. Although some core-shell type carriers could encapsulate dual drugs in the core and shell regions, respectively,[13] drug loading efficiencies were low. In addition, the volume of carrier is likely expansion with the increase of types and upload amount of drugs. It will be disadvantage because big particles ($>$200 nm) easily trigger phagocytosis of macrophage or interception of internal membrane system in vivo.[14] Hence it is critical to develop a kind of desired carrier to upload various drugs to relatively separate space on the vehicle.

Photothermal therapy with near-infrared (NIR) irradiation can also avoid the occurrence of anticancer drug resistance, and has motivated extensive research interest due to its minimal invasiveness compared with other cancer interventions.[15] Currently, various superparamagnetic

nanoparticles-based multifunctional nanocomposites have been widely developed as photothermal therapy agents.[16,17] It is particularly significant to induce the tumor necrosis based on the concept that magnetic nanoparticles, when exposed to a NIR laser beam, convert the irradiation energy into heat capable of killing tumor cells in vivo.[18] Magnetic drug delivery system is promising in comprehensive application of tumor-targeted chemotherapy and hyperpyrexia.[19,20] On the basis of our previous works, it would facilitate high-accuracy and internalization treatment of tumor when external magnetic induction is integrated with cell endocytosis technology.[21,22] Thus it can be seen that the combination of multidrug synergic treatment, photothermal therapy, and magnetic targeting is a multi-modal strategie against tumors.

Recently, novel grapheme oxide (GO)-based nanocomposites have been given much attention in a variety of biomedical applications, including drug delivery,[23] gene delivery,[24] and imaging.[25] Graphene oxide moiety in the hybrids possesses large specific surface area, monoatomic layer plane structure and abundant hydroxyl, carboxyl or epoxy groups.[26] These excellent characteristics allow it to have not only strong π-π interactions with the aromatic rings existing in many drug molecules but also capability to conjugate drug molecules by forming new chemical bond or electrostatic attraction.[27] Thus far, however, little has been done to explore the performance of GO-Fe_3O_4 composite in multi-drug delivery, despite much effort in the combination of single drug delivery with other functions such as photothermal therapy and magnetic resonance imaging for in vitro and in vivo antitumor applications.[28] In addition, in the existing GO-Fe_3O_4 composites prepared by chemical deposition method, the amount of Fe_3O_4 MNPs captured on hybrid was so low that the magnetic responsiveness was insufficient to the guidance of external magnetic field,[29] which would affect the application in biomedical field.

Herein, we synthesized an alternative GO@Fe_3O_4 composite to orderly bind camptothecin and methotrexate to this carrier (Fig. 1). Subsequently, we researched the efficacy of combination of dual-drug chemotherapy and photothermal therapy in a mouse drug-resistant S-180 sarcoma model. The results indicated that combining dual-drug chemotherapy with photothermal therapy could enhance tumor drug resistance reversal by activating multiple anticancer mechanisms.

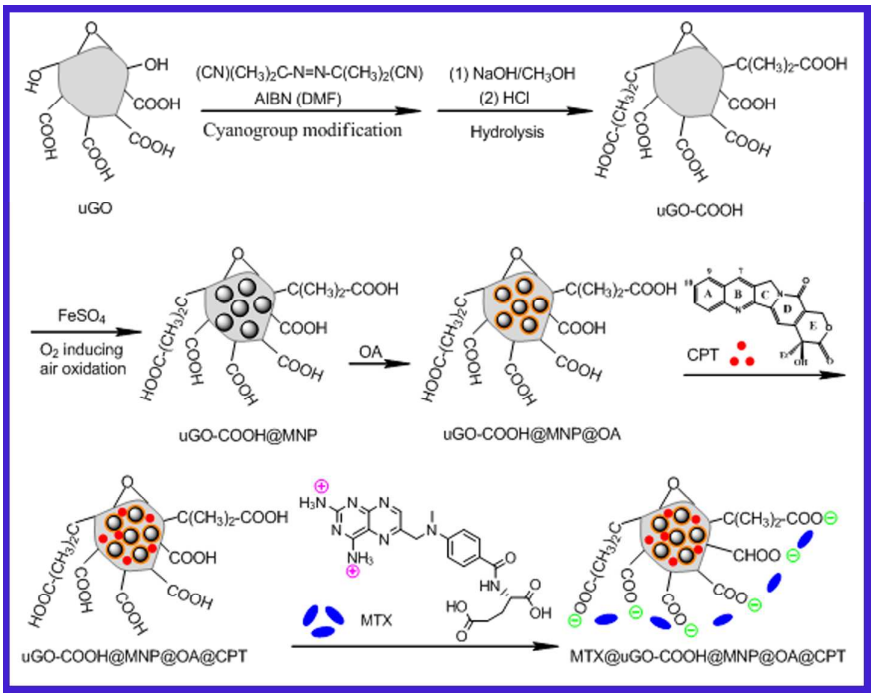

Fig. 1. Schematic diagram showing the preparation of a MTX@uGO-COOH@MNP@OA@CPT nanocomposite.

2. Materials and methods

2.1. Materials

Graphite (99.95%) with an average particle diameter of 4 mm, 98% sulfuric acid, sodium nitrate, potassium permanganate, hydrogen peroxide, dimethyformamide (DMF), azodiisobutyronitrile (AIBN), oleic acid (OA), iron sulfate heptahydrate, sodium hydroxide, camptothecin (CPT), methotrexate (MTX) were acquired from Sigma Aldrich (Shanghai, China). Dimethyl sulfoxide (DMSO) was provided by Gansu Yinguang Chemical Industry Co. (China). The AIBN was processed by recrystallization and stored in a cool dry place. All the other reagents were analytical grade and used as received without further purification. All cell lines used in experiment were acquired from the cell bank (China). The ultrapure water was used throughout the experiment.

2.2. Preparation of ultra-fine GO (uGO)

Ultra-fine graphene oxide (uGO) sheets were prepared from expandable graphite powder by a modified Hummers method.[30] Briefly, expandable graphite powder (10 g) was ground with sodium chloride (50 g) for 10 min. Then the mixture was dissolved in water to remove sodium chloride by centrifugation. The precipitation was dried at 50 ℃. The ground graphite sheet (5 g) was preprocessed with 120 mL of concentrated sulfuric acid in a 500 mL round bottom flask under

ultrasonication for 40 min. Then 2.5 g of sodium nitrate were added to the suspension. Fifteen grams of potassium permanganate were gradually added to the ingredients in an ice bath under vigorous stirring. After that, the temperature of the suspension was rose to 60 ℃, where it was maintained for 40 h. Next, water (250 mL, 60 ℃) was added, and the mixture was boiled for 15 min and further diluted to approximately 1000 mL with boiling water. The reaction was terminated by the addition of 30% H_2O_2 solution (50 mL). The product was washed first with 5% HCl solution and then with deionized water (250 mL, 60 ℃) until complete removal of the residual salts and acids. The filter cake was dried at 50 ℃ and denoted as graphene oxide (GO). The resulting GO (500 mg) was re-dispersed in 1500 mL of deionized water to acquire a brown suspension and sonicated (200W) for 60 min to strip GO. The mixture was centrifuged at 10000 rpm for 10 min at 25 ℃. The precipitation was denoted as uGO and dispersed in 10 mL of deionized water by sonication. The resulting uGO suspension (2 mL) was carefully added on the surface of three layers of sucrose that the successive order of mass concentration was 60%, 45%, and 30% (10 mL each) from bottom to top in a centrifuge tube. The ultracentrifugation was conducted at 60000 rpm for 2.5 h at 25 ℃. The three layers stratified by the density gradient method were collected and washed thoroughly with deionized water to remove sucrose, respectively. The products were dried at 50 ℃ and denoted as L1-uGO, L2-uGO and L3-uGO.

2.3. Carboxyl modification of uGO

The as-prepared uGO nano-sheet (100 mg) from the different layer was dispersed into 80 mL of DMF by ultrasonication for 30 min, respectively. The recrystallization azodiisobutyronitrile (AIBN) was added to the suspension by a mass ratio of uGO: AIBN=1:50. The mixture was stirred for 5 h under protection of nitrogen at 70 ℃. The intermediate product uGO-C$(CH_3)_2$CN was collected by vacuum filtration and washed three times with DMF and dried overnight at 40 ℃. Then 50 mg of uGO-C$(CH_3)_2$CN were dissolved in 50 mL of CH_3OH solution containing NaOH (10 mol/L). The mixture was maintained at 90 °C in an oil bath and stirred strongly under reflux for 48 h. After the flask was cooled to room temperature, the pH of the aqueous solution was adjusted to 3.0 by HCl (1 M). The products uGO-C$(CH_3)_2$COOH (denoted as L1-uGO-COOH, L2-uGO-COOH, L3-uGO-COOH) were repeatedly washed with deionized water until the solution became neutral. Their contents of carboxylic groups were determined by acid-base titration as reported in literature,[29] and their zeta potentials were measured.

2.4. Synthesis of uGO-COOH@MNP@OA hybrid

L2-uGO-COOH was used as a substrate for MNPs growth giving uGO-COOH@MNP hybrids. In a typical reaction, 600 mg of L2-uGO-COOH was dispersed in NaOH solution (0.23 mol/L, 35 mL) by ultrasonication and stirred for 48 h under nitrogen. Then 2.919 g of iron sulfate heptahydrate was dissolved to the suspension under stirring. The suspension was immediately adjusted to pH=8.6 with NaOH solution, followed by stirring for 24 h. Afterwards, iron ions were oxidated for 3 min in oxygen delivered at a flow rate of 0.04 m^3/ h and for another 10 min in air delivered at a flow rate of 0.1 m^3/ h by keeping shaking. The suspension was re-adjusted to pH=10.0 with above NaOH solution and further reacted for 1 h under mechanical stirring. The product (uGO-COOH@MNP) was collected and washed thrice with deionized water to remove precursors. The MNP surface was grafted further with 4.5 mL of oleic acid (OA) in an oil bath at 80 °C for 20 min under nitrogen.[27] The resulting uGO-COOH@MNP@OA hybrid was washed thrice with acetone and dried in a freezer dryer.

2.5. Characterization

Transmission electron microscopy (TEM, FEI, TecnaiG^2 F30, USA), scanning electron microscopy (SEM, Hitachi, S-4800, Japan), dynamic light scattering (DLS, BI-200SM, USA) with angle detection at 90º were used to characterize the morphology and size of the composite. The zeta potentials of composite (500 μg/mL) at different pH and media were recorded on a Zetasizer (Nano 3600, Malvern, U.K.) in triplicate. FTIR spectra were acquired with a FTIR spectrometer (NEXUS 670 FT-IR, Nicolet, USA). The magnetization curve of the uGO-COOH@MNP@OA hybrid was recorded using a vibrating sample magnetometer (VSM) (Lake Shore, USA) at 300 K. The composition of the hybrid was determined with thermal gravimetric analysis (TGA) on a Perkin-Elmer 7-series/UNIX with a heating rate of 10 ℃/min from room temperature to 1000 ℃ under N_2 protection.

2.6. Dual-drug loading and release

Anticancer drug camptothecin (CPT) and methotrexate (MTX) were selected. Their loading was accomplished as follows: (1) 50 mg of uGO-COOH@MNP@OA hybrid were dispersed in 50 mL of CPT solution (1 mg/mL in DMF) by ultrasonication for 40 s, and vibrated overnight at 4℃ until CPT content in the solution was invariant. CPT-loaded composite was separated by centrifugation at 6000 rpm for 5 min and rinsed three times with DMF to remove excess CPT. (2)

above composite was mixed with 50 mL of MTX solution (1 mg/mL in PBS, 50 mM, pH 7.4) and immediately vortexed at high speed for 60 s. The mixture was kept at room temperature for 30 min, and then separated by centrifugation at 6000 rpm for 5 min and washed thrice with PBS to remove unbound MTX, followed by freeze drying. All the supernatants in above two steps were collected to assay the amounts of unbound drugs at 366 nm for CPT and at 302 nm for MTX by UV-visible spectrophotometer. The loading efficacy and loading amount of CPT and MTX were determined based on the decrease in initial addition. The experiments of dual-drug loading were carried out in triplicate.

The drug-release pattern of MTX@uGO-COOH@MNP@OA@CPT composite was determined by a dialysis method in a simulated normal body fluid (PBS, 50 mM, pH 7.4) and an acidic medium (PBS, 50 mM, pH 5.3). Briefly, 50 mg of the MTX@uGO-COOH@MNP@OA@CPT composites were dispersed in 5 mL of medium and transferred to a dialysis tube. The dialysis tube was immersed in 45 mL of the corresponding medium in a water bath at 37±1℃ with gentle shaking. 200 microlitre of the release medium were withdrawn for the UV-visible absorption assay of the amount of CPT and MTX and substituted with 200 μL of fresh PBS at regular intervals. Each sample was analyzed in triplicate and results were presented as mean (standard deviation).

2.7. Cytotoxicity, flow cytometry and hemolysis assay

Human hepatocytes cancer HepG2 cells and normal hepatocytes L02 cells were seeded in 96-well plates at a density of 1×10^4 cells/well in 200 μL of RPMI-1640 medium supplemented with 10% fetal calf serum and 1% penicillin/streptomycin at 37 °C with 5% CO_2 for overnight, respectively. The cells were then incubated with the MTX@uGO-COOH@MNP@OA@CPT composite with a concentration from 10 to 500 μg/mL for another 24 h, respectively. The cell viabilities were assayed using MTT method as reported.[18] As a comparison, empty uGO-COOH@MNP@OA hybrid and only CPT- or MTX-loaded uGO-COOH@MNP@OA composites were also used for evaluation of the cytotoxicity under similar condition. For the detection of composite-induced apoptosis, the cells treated with the different composites were stained with FITC-labeled Annexin-V and propidium iodide (PI) and detected in the flow cytometer (BD LSRFortessa, USA). In order to compare with free drug-induced apoptosis, HepG2 cells treated with free CPT and free CPT@MTX corresponding to the concentration loaded in hybrids were also detected. The cell micro-structure observation was also been conducted by a

LSCM (510 Meta, ZEISS, Germany, Ex=488 nm). All experiments were conducted in triplicate.

In order to assess hemocompatibility of the CPT@uGO-COOH@MNP@OA@MTX composite, hemolysis assay in vitro was also done. The content was presented in SI 1.

2.8. Magnetic guidance and drug-coupled photothermal therapy in vivo

All experiments were carried out according to the protocols approved by the Ethics Committee of Animal Experiments of Lanzhou University. Briefly, S-180 murine sarcoma cells (2×10^6 cells/0.2 mL) were inoculated to the right front oxter of each male Balb/c mice (4–6 weeks old). On day 6 after tumor cell transplantation, the mice were randomly divided into eight groups (n = 5/group): control (group 1), MTX@uGO-COOH@MNP@OA@CPT (groups 2 and 3), uGO-COOH@MNP@OA@CPT (group 4), MTX@uGO-COOH@MNP@OA (group 5), and three free drug groups (groups 6-8). Then, the mice from nanocomposite group 2, 3, 4, and 5 were treated with suspension containing composites in sterile PBS irradiated by ^{60}Co by a lateral tail vein (0.2 mL per mouse, 2 mg/kg body weight) every other day for 14 days, respectively. The mice from free drug group 6, 7, and 8 were treated with CPT, MTX and their combination corresponding to the CPT and MTX concentration loaded in nanocomposites in sterile PBS at the same pattern (0.2 mL per mouse), respectively. The control group mice were given 0.2 mL of sterile PBS. As soon as injection was achieved, the mice were anesthetized using isoflurane and covered with tin foil paper, leaving inoculation site exposed, followed by inducing for 4 h with a constant magnet field (about 2000 Oe) and subsequent irradiating for 20 min using a near-infrared laser spot (diameter=10 mm, 2 W) on the tumor site at 25 °C. The mice from group 2 were induced without irradiating. On day 14, all the mice were sacrificed and tumor tissues were removed. Tumor inhibition rate was determined by the following formula: tumor inhibition rate = (the average tumor weight of the control group－the average tumor weight of treatment group)/the average tumor weight of the control group×100%.[31] We chose this equation because it was used for calculating the tumor inhibitory rate based on tumor mass. We think that it is more reasonable to calculate the tumor inhibitory rate on the basis of the tumor mass than the volume.

2.9. In vivo targeting assess

MTX@uGO-COOH@MNP@OA@CPT composite was labeled with rhodamine B (Rh B) to trace its bio-transportation by fluorescent probe. Labeling method was described in SI 2. The male S-180 sarcoma-bearing Balb/c mice were anesthetized with 2.5% isoflurane in oxygen delivered at

a flow rate of 1.5 L/min. Rh B-labeled MTX@uGO-COOH@MNP@OA@CPT composite was injected and induced in vivo as described in the section 2.8. Then the bio-fluorescence in vivo imaging was monitored at specified time points using the IVIS Imaging System (Xenogen Co., Alameda; Ex= 570 nm, Em= 650 nm). All images were normalized and analyzed using Living Image 3.2 software. In order to confirm further accumulation of nanocomposites in tumor, the mice induced for 4 h were killed, and the tumor tissues were quickly removed and fixed with 4% paraform for 48 h. After dehydrated progressively, the fixed sections were embedded in paraffin, sectioned, and stained with H&E and Prussian Blue standard protocol.

3. Results and discussion

3.1. Synthesis of uGO-COOH@MNP@OA composites

Synthesis of uGO-COOH@MNP@OA composites consisted of the following three steps. In the first step, in order to modify more carboxyl groups on uGO sheets stripped, we firstly separated uGO sheets by size. We used a density gradient ultracentrifugation method in which sucrose was selected as an inert medium. Three sized uGO sheets (L1-uGO, L2-uGO, L3-uGO) in a density gradient were obtained by collecting suspension in different zones (Fig. 2A). SEM images of different fractions clearly presented morphology and size distribution (Fig. 2B-D). Obviously, the fractions in the upper possess smaller sizes and thinner sheets than those in the lower, suggesting uGO has been successfully separated. Then, a free radical initiator azodiisobutyronitrile (AIBN) was employed as a functional modifier. AIBN would decompose and generate isobutyronitrile radicals that attacked on the defects of five- and seven-membered rings in uGO, which formed cyanogroup-modified uGO-C$(CH_3)_2$-CN. This intermediate further produced carboxyl-modified uGO-C$(CH_3)_2$-COOH (abbreviated as L1-uGO-COOH, L2-uGO-COOH, L3-uGO-COOH) through hydrolysis reaction in NaOH/CH_3OH solution. According to the determination of carboxyl group contents in three fractions (Fig. 2E), the smaller the uGO-COOH sheets were, the higher the amount of carboxyl functional groups was. This may be because smaller uGO-COOH sheet possessed larger specific surface area, more carboxyl exposure accordingly. In addition, compared with the amount of carboxyl groups of three uGO-COOH precursors, the contents of carboxyl functional groups of L1-uGO-COOH, L2-uGO-COOH, and L3-uGO-COOH fractions increased 1.8, 1.5, and 1.4 fold, respectively (Fig. 2E).

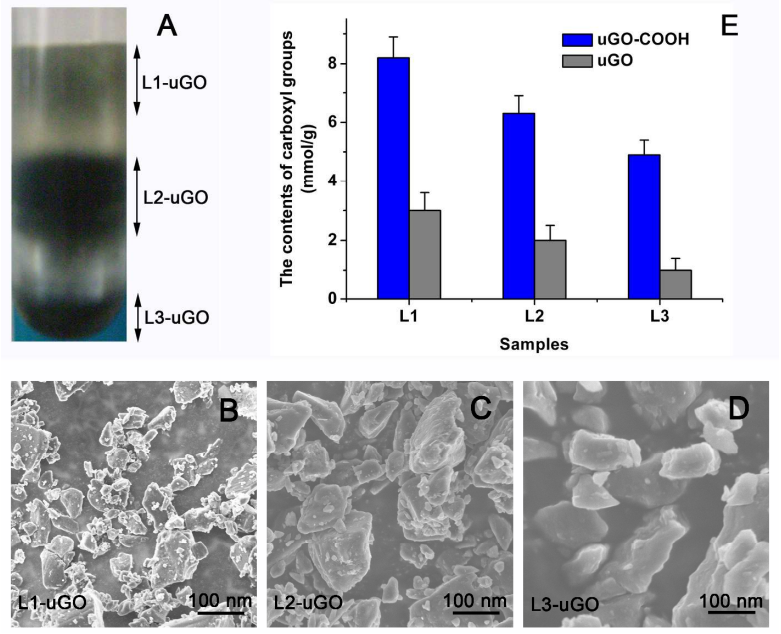

Fig. 2. (A) Photograph of three layers of uGO fabricated by ultrasonic stripping and density gradient ultracentrifugation. (B-D) SEM images of uGO sheets from the different layers as marked in (A). (E) The contents of the carboxyl groups from the different uGO layers before and after carboxylation.

The zeta potential values showed that carboxyl group-modified uGO possessed higher negative ζ potential of about -46.6 mV (L1-uGO-COOH), -39.4 mV (L2-uGO-COOH) and -28.5 mV (L3-uGO-COOH) than uGO (-17.8 mV) in PBS, respectively (Table 1). Their high negative ζ potential values further confirm the presence of more carboxyl groups on the uGO-COOH surface due to the stripping process and carboxyl modification. Carboxyl-functionalized graphene oxide make it negatively charged surface, which possesses excellent chemical activities and infiltration properties, and may facilitate to capture both metal ions including iron ions by coordination bonding and drug molecules by electrostatic attraction. So, this high carboxyl content of uGO provided platform for the subsequent loading of MNPs and anti-cancer drug.

Table 1. Zeta potentials of the different samples in PBS (pH 7.4)

Samples	Zeta potential (mV)
L1-uGO-COOH	-46.6±4.2
L2-uGO-COOH	-39.4±3.3
L3-uGO-COOH	-28.5±2.8
uGO	-17.8±2.2
uGO@MNP@OA	-26.5±2.9
uGO-COOH@MNP	-31.5±3.4
uGO-COOH@MNP@OA	-53.4±4.5

In the second step, superparamagnetic uGO-COOH@MNP hybrid was synthesized by the combination of a simple and effective chemical deposition of iron ions on uGO-COOH sheets with their further oxidation (Fig. 1). Firstly, L2-uGO-COOH was selected as the starting materials in the synthesis of hybrid in consideration of suitable size and high yield of uGO-COOH. After the pH of the aqueous $FeSO_4$ solution was adjusted to 8.6 at room temperature, Fe^{2+} ions were bound to carboxylate anions on the uGO-COOH sheets by coordinate bond. At the same time, Fe^{2+} ions were turned into $Fe(OH)_2$ in alkaline environment. Then, $Fe(OH)_2$ was oxidated into Fe_3O_4 nanoparticles through O_2 inducing and air slow oxidation processes in aqueous NaOH solution (pH=10), which the black Fe_3O_4 nanoparticles were precipitated in the uGO-COOH sheet.

In the third step, to efficiently promote the dispersibility of the uGO-COOH@MNP hybrid and the loading of CPT in organic solvent,[27] the surfaces of the Fe_3O_4 nanoparticles on the uGO-COOH sheets were coated with the OA molecules.

3.2. Characterization

The dispersibility and zeta potential of the composites should be measured in such relevant physiological media as human serum albumin (HSA)-containing PBS because the protein adsorption effect could significantly modify these parameters. In order to simulate physiological media for these data analysis, a HSA (0.6 mM)-containing PBS solution was used because albumin is the most abundant protein that generally occupies a concentration of 0.6 mM in serum.[19,32] The results showed that, in the absence of HSA, the mean diameter of the uGO-COOH@MNP@OA was measured to be approximately 80±20 nm in PBS at pH 5.3 and pH 7.4 by DLS (Fig. 3A). In the presence of HSA, the particle size magnified 10 nanometers at pH 5.3, but there was only a little bit of fluctuation of this data at pH 7.4 (Fig. 3B). This may be that the adsorption effect between HSA molecules and the nanoparticles became stronger at pH 5.3 than at pH 7.4. The results of zeta potentials in HSA-containing PBS were not listed in the manuscript because of limited layout, but were presented in SI 3.

The TEM images (Fig. 3C) under low magnification confirm that uGO-COOH@MNP@OA hybrid possesses a particle sizes about 70-90 nm. The morphology of the uGO-COOH@MNP@OA nanohybrid characterized by TEM in Fig. 3C and 3D distinctly demonstrates that Fe_3O_4 MNPs of less than 20 nm in size are uniformly immobilized onto the uGO-COOH sheets. The morphology of the resulting uGO-COOH@MNP@OA hybrid was also

showed in SEM image (Fig. 3E). Obviously, uGO sheets were inlaid with Fe_3O_4 MNPs, which was consistent with the results observed from the TEM. All these results indicate the successful preparation of uGO-COOH@MNP@OA hybrid.

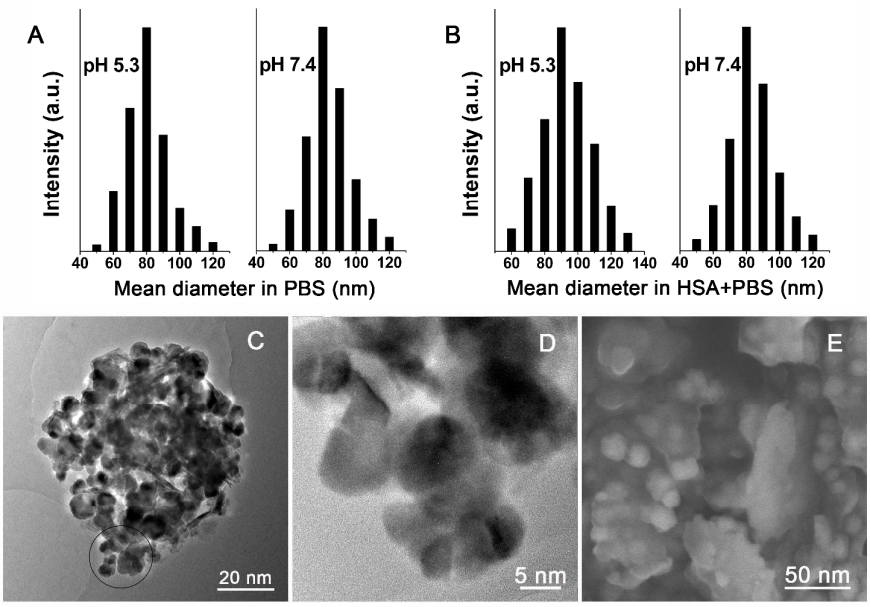

Fig. 3. (A) and (B) The particle size distributions of uGO-COOH@MNP@OA nanocomposite in PBS and HSA (0.6 mM)-containing PBS media at pH 5.3 and pH7.4. (C) and (D) Low and high magnification TEM images of uGO-COOH@MNP@OA nanocomposite. The highlight section with black color in (C) is magnified in (D). (E) SEM image of uGO-COOH@MNP@OA.

Fig. 4A illustrates the precise mass loss of the resulting uGO-COOH@MNP@OA hybrid as the temperature increased in a nitrogen environment. It is observed that uGO-COOH@MNP@OA hybrid presented a 12% mass loss at about 100 ℃, indicating the vaporization of the residual or absorbed solvent. The obvious weight loss occurred around 300 ℃ may be attributed to the pyrolysis and escape of OA and different functional groups on uGO-COOH. The sharp weight loss at the initial point of 720 ℃ implied the fracture of the carbonaceous support, such as carbon skeleton of uGO-COOH and carboxyl group coordinated with Fe_3O_4 MNPs. This is similar to the preparation of superparamagnetic graphene oxide nanoparticles hybrid in the previous report.[29,32] A 54.2% mass loss of uGO-COOH@MNP@OA at 780 ℃ and almost no weight loss hereafter suggested that the remaining 45.8% of the hybrid were derived from MNPs. This result is consistent with that calculated from the content of iron by atomic absorption spectrum. The TGA of carboxyl group-unmodified uGO@MNP@OA is used as a comparison, as shown in Fig. 4A. Only 36.6% of the hybrid was derived from MNPs. This difference indicates that the introduction

of more carboxyl groups is advantageous to the immobilization of MNPs. Furthermore, the upload capacity of Fe_3O_4 MNPs in uGO-COOH@MNP@OA nanohybrid is significantly much higher as compared with the GO–Fe_3O_4 hybrid prepared by other chemical precipitation method, where this data is estimated only 18.6 wt%.[32]

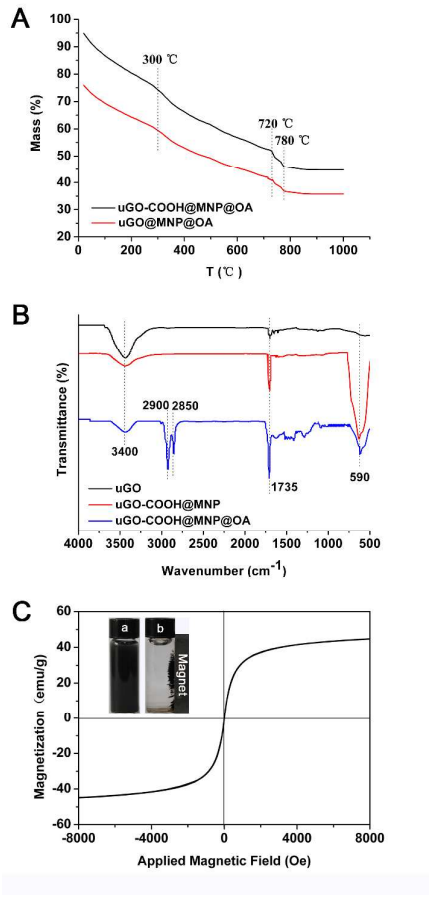

Fig. 4. (A) Thermal gravimetric analysis, (B) FTIR spectra, and (C) magnetization curve of hybrids or their ingredients. The inset in left top in (C) show photographs of (a) before and (b) after uGO-COOH@MNP@OA hybrid was attracted by a magnet in deionized water.

The composition of uGO-COOH@MNP@OA hybrid was further characterized with FTIR, as shown in Fig. 4B. Compared with carboxyl-unmodified uGO, the characteristic peak corresponding to the stretching vibration of hydroxy group at 3400 cm^{-1} in uGO-COOH@MNP hybrid has significantly weakened. On the contrary, the peak related to the carbonyl group from uGO-COOH@MNP at 1735 cm^{-1} became stronger. These results clearly verified that the hydroxy groups on uGO have been successfully turned into carboxyl groups after carboxyl modification. Moreover，uGO-COOH@MNP hybrid showed a peak at 590 cm^{-1}, which corresponds to the

stretching vibration of Fe−O bond in pure Fe_3O_4, reflecting the presence of Fe_3O_4 MNPs in the composite. The FTIR spectra of the uGO-COOH@MNP@OA hybrid presented two sharp peaks of methylene group at 2900 cm^{-1} and 2850 cm^{-1}, and a stronger peak of carbonyl group at 1735 cm^{-1}, which is presumably due to the introduction of oleic acid. In addition, the special peak corresponding to the Fe−O bond at 590 cm^{-1} weakened, suggesting that Fe_3O_4 MNPs on uGO-COOH sheets have been expectably coated by oleic acid.

The magnetization property of uGO-COOH@MNP@OA hybrid was recorded at room temperature, as shown in Fig. 4C. Although the saturation magnetization intensity weakened compared with that of pure Fe_3O_4 MNPs (79 emu/g, in our previous report) due to the introduction of uGO-COOH and OA, the value still occupied about 46 emu/g.[21] This data is significantly much higher than that reported in the literature,[29] where the saturation magnetization was merely 4.62 emu/g because of the low loading amount of Fe_3O_4 on GO. According to the photographs of the inset in left top in Fig. 4C, uGO-COOH@MNP@OA hybrid can be completely attracted by a magnet. This suggests the resulting uGO-COOH@MNP@OA hybrid can perfectly meet requirements of magnetic induction and hyperthermia for the use in vivo.

3.3. Encapsulation efficiencies and release of CPT and MTX

The encapsulation efficiencies of CPT and MTX are presented in Fig. 5A. The loading of CPT was achieved by π–π stacking between uGO and CPT. Its saturated loading amount on uGO-COOH@MNP@OA hybrid is 682 mg/g (Fig. 5A(c)). As two comparison, the loading amounts of CPT on L2-uGO-COOH and uGO-COOH@MNP were determined to be 950 mg/g and 366 mg/g at the same initial CPT concentration, respectively (Fig. 5A (a, b)). This may be because some surface areas on L2-uGO-COOH have been occupied by MNPs, which caused the loading amounts of CPT on uGO-COOH@MNP hybrid is less than that on L2-uGO-COOH. However, when MNPs on uGO-COOH@MNP hybrid were coated by OA, the loading amount of CPT rose again to 682 mg/g. The OA shell on MNPs surface provided a reservoir to enrich the hydrophobic drug. Such an amount of loading was higher than that of the other multifunctional magnetic nano hydrogel previously prepared by us,[22] where the loading capacity of CPT was only 70.2 mg/g. In the case of MTX, the loading of MTX on uGO-COOH@MNP@OA hybrid was realized by electrostatic attraction between carboxyl anions on uGO or OA and amino cations of MTX. The zeta potentials of uGO-COOH@MNP@OA, L2-uGO-COOH, uGO-COOH@MNP,

and uGO@MNP@OA were -53.4±4.5, -39.4±3.3, -31.5±3.4, -26.5±2.9 mV, respectively (Table 1). Obviously, the highest loading capacity of MTX was found in uGO-COOH@MNP@OA (896 mg/g)＞L2-uGO-COOH (599 mg/g)＞uGO-COOH@MNP (446 mg/g)＞uGO@MNP@OA (256 mg/g) (Fig. 5A blue column). This shows that the loading capacity of MTX heavily depends on the contents of $-COO^-$ on nanocomposite surface.

The drug release kinetics from the MTX@uGO-COOH@MNP@OA@CPT in vitro with change of pH was explored. As shown in Fig. 5B, the MTX release is always faster than CPT in PBS at pH 5.3 and pH 7.4. The amount of released MTX reached approximately 60% at pH 5.3 and 49% at pH 7.4 within 40 h. However, CPT release always slowly continued in two kinds of media. On the one hand, the discrepancy of release profiles can be attributed to the different loading patterns of MTX and CPT. When the pH of the medium changed, the charges on uGO and MTX would accordingly change. MTX molecules loaded in the form of electrostatic attraction would rapidly break away from MTX@uGO-COOH@MNP@OA@CPT composite. By contrast, the amount of released CPT was only 21% at pH 5.3 and 15% at pH 7.4 even if dialysis was prolonged to 72 h (Fig. 5B). The release profile verifies the stability of CPT on uGO-COOH@MNP@OA hybrid because CPT was closely bound to the surface of graphene sheets via strong aromatic ring stacking and hydrophobic force. The slow CPT release profile was very the same as that of reported chitosan-functionalized GO-based drug carrier, where it took 72 h to release 17.5% of CPT.[33] On the other hand, the MTX molecule has two NH_2 groups, so its water solubility is stronger than that of CPT, which can illustrate why the release ratios of MTX were about 3 times at pH 5.3 and 3.6 times at pH 7.4 that of CPT within 72 h, respectively.

Furthermore, the MTX and CPT cumulative releases from MTX@uGO-COOH@MNP@OA@CPT composite were higher at pH 5.3 than at pH 7.4 (Fig. 5B). In the case of MTX, a possible reason may be that electrostatic attraction between uGO-COO^- and MTX-NH_3^+ were easier to be destructed under acidic condition than the neutral condition, causing faster release of MTX. In addition, the solubility of MTX at pH 4～5.5 is optimum, which led to more favorable release at pH 5.3 than that at pH 7.4. In the case of CPT, it was likely that the quinoline ring (B ring) in CPT molecule (insert in Fig. 1.) was extremely easy to generate positively charged salt under acid condition (pH 5.3), which resulted in not only decrease of binding force between CPT and uGO but also mutual repulsion between CPT and the protonized

uGO-COOH. Similar drug release profile has been observed previously for sulfonic acid groups-functional GO.[34] The pH-dependent drug release from MTX@uGO-COOH@MNP@OA@CPT composite is exactly what we expect, i.e., anticancer drugs MTX and CPT could mainly be released around tumor tissues (acidic microenvironment). In other words, they were relatively stable on composite in the blood-stream before arriving at the targeted tumor site, which would potentially magnify chemotherapy efficacy and lessen toxic and side effect.

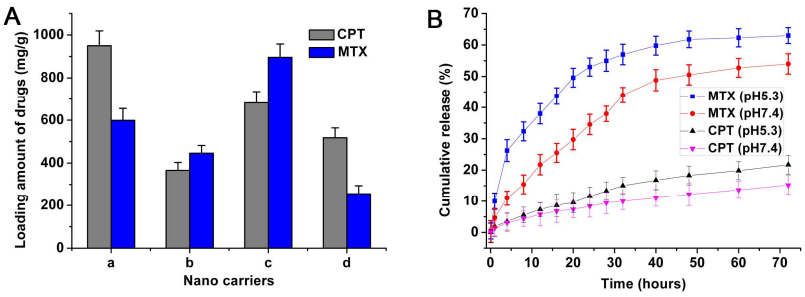

Fig. 5. (A) Loading capacities of CPT and MTX on (a) L2-uGO-COOH, (b) uGO-COOH@MNP, (c) uGO-COOH@MNP@OA, and (d) uGO@MNP@OA. (B) Release profiles of CPT and MTX from MTX@uGO-COOH@MNP@OA@CPT in PBS (50 mM, pH 5.3 and pH7.4).

3.4. In vitro cytotoxicity

As shown in Fig. 6, empty carrier revealed high cell viabilities for HepG2 cells (82%) and L02 cells (83%) even at a high concentration of 500 μg/mL, indicating that the carriers possessed good biological compatibility. However, the drug-loaded composites showed obvious growth inhibition activity for both cancer and normal cells. The increased efficacy should be attributed to the contribution of the drugs bound on uGO-COOH@MNP@OA hybrid. Particularly, MTX@uGO-COOH@MNP@OA@CPT composites presented lower cell viability for two kinds of cells than single drug-loaded composites, indicating the former is highly potent to synergistically kill cells (Fig. 6 A, B). In vitro cell viabilities of cancer cells have been compared with that of normal L02 cells (Fig. 6A, B). The results suggested that cancer cells presented slightly lower cell viability than normal cells at the same concentration of dual drug-loaded composites, reflecting that compared with normal cell, cancer cells were more vulnerable to dual drug-loaded composites in vitro. In the case of free drugs, CPT and CPT@MTX showed different cytotoxicities to HepG2 cells (Fig. 6C). The higher cytotoxicity of CPT@MTX may be attributed

to the synergistic effect of two drugs in comparison with that of sole CPT.

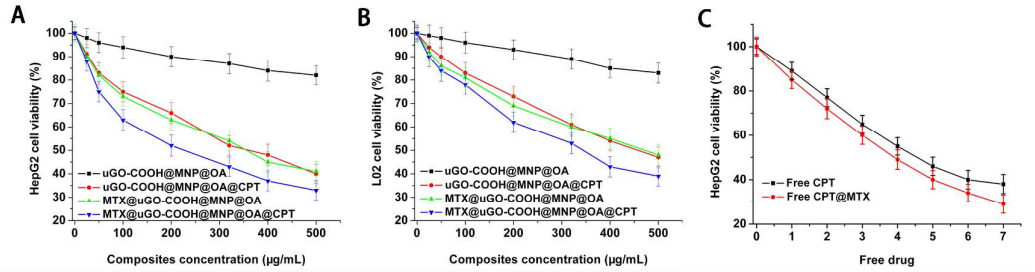

Fig. 6. In vitro cell viabilities of the different composites at the different concentrations against HepG2 cells (A) and L02 cells (B), respectively. (C) Cell viabilities of free CPT and free CPT@MTX corresponding to each concentration point in (A) loaded on CPT@uGO-COOH@MNP@OA@MTX composite against HepG2 cells.

3.5. Quantitative and qualitative apoptotic assay

As is showed in Fig. 7A., HepG2 cells untreated with drugs or composites hold a 95.01% of living cell (Q4), and negligibl dead cells (Q1) and apoptotic cells (Q2+Q3). However, free CPT induced 2.68% of dead cells (Q1) and 58.15% of apoptotic cells (Q2+Q3) (Fig. 7B), while the free CPT+MTX could increase dead cells to 36.22% (Fig. 7C), which may be attributed to the synergistic effect of two kinds of drugs. In contrast, only CPT-loaded uGO-COOH@MNP@OA@CPT composites induced 4.91% of dead cells (Q1) and 49.14% of apoptotic cells (Q2+Q3) (Fig. 7D), suggesting that the CPT released from the composite still possessed the similar anticancer activity as free CPT. Furthermore, it can be observed that dual drug-loaded MTX@uGO-COOH@MNP@OA@CPT composite led to approximately two-thirds cells death and apoptosis (Q1+Q2+Q3=66.84%) (Fig. 7E), reflecting that the CPT and MTX released from the composite still possessed the synergistic anticancer effect. Most importantly, the drugs were protected by carrier all along before composite directly released drug into cytoplasmic matrix, so that apoptosis was more effectively induced than free drugs in vivo.

In order to further investigate apoptosis mechanism, HepG2 cells co-stained with annexin V/PI after treated with MTX@uGO-COOH@MNP@OA@CPT composite were detected by LSCM. It can be clearly seen (Fig. 7F) that the cellular membrane and matrix have showed green fluorescence from annexin V-FITC that can only react with phosphatide acyl serine inside membrane, suggesting that membrane has been damaged and cell has been apoptosis. In addition, red fluorescence nucleus further confirm the cell have been at later period of apoptosis even death because propidium iodide (PI) can only stain dead cell. All these demonstrated that the resulting

composites have successfully induced apoptosis and possess the potential to effectively inhibit tumor growth.

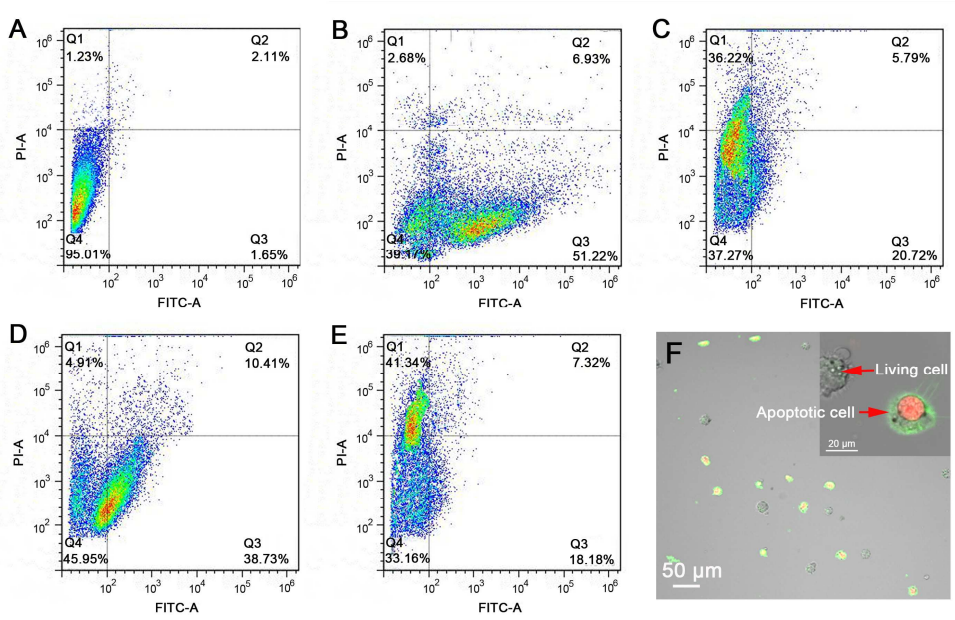

Fig. 7. (A) Control of HepG2 cells untreated. Apoptosis analysis of HepG2 cells after treated with (B) free CPT and (C) free CPT+MTX corresponding to the CPT and MTX loaded on hybrids, and (D) uGO-COOH@MNP@OA@CPT, (E) MTX@uGO-COOH@MNP@OA@CPT composites in sterile PBS. (F) Representative HepG2 cells co-stained with annexin V/PI after treated with MTX@uGO-COOH@MNP@OA@CPT composite. The inset in right top in (F) shows high magnification cell image.

3.6. In vivo tumor targeting characteristics of composite

To achieve the visual demonstration that the MTX@uGO-COOH@MNP@OA@CPT composite could target to tumor tissue in vivo under magnetic induction, the composite was labeled with Rh B as a fluorescent tracer. The results show that the uptake of the Rh B-labeled MTX@uGO-COOH@MNP@OA@CPT originally exhibited in the intraperitoneal organs (Fig. 8A). The distribution of the composite was more homogeneous. There was not apparent fluorescence in the tumors at magnetic guide 2 h post-injection. But as the magnetic induction continued, the composite gradually accumulated in the tumor but not in most normal tissues. It only took about 4 h to finish tumor accumulation, indicating potential accumulation capability of MTX@uGO-COOH@MNP@OA@CPT in the tumor tissue under magnetic guidance. According to the previous reports, it took 72 h to target conjugates to tumor after i.v. administration.[35,36] Such a long circulation of carrier is very disadvantage because CPT molecule on vehicle is easy to transform from the lactone to carboxylate in the bloodstream, which leads to a complete loss of

anticancer activity.[37] Therefore, even though the present composite was not modified using targeting ligand moiety, it still achieved high specific accumulation within a relatively short time under magnetic guidance, which mainly thanks to the high encapsulation efficiency of Fe_3O_4 MNPs and sensitive magnetic responsiveness. Prussian blue staining of the tumor slice was also clearly observed that Fe_3O_4 MNPs were uniformly and significantly scattered within the tumor tissue, further indicating the success of specific accumulation after induced for 4 h (Fig. 8B).

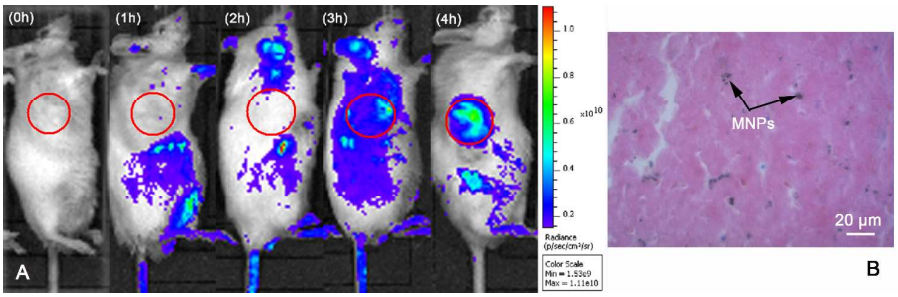

Fig. 8. (A) Typical in vivo images of the male S-180 sarcoma-bearing Balb/c mice that have undergone magnetic guide at defined time periods (0, 1, 2, 3, and 4 h) post-intravenous injection of RhB-labeled MTX@uGO-COOH@MNP@OA@CPT composite. The highlight sections with red color are tumor sites. The system uses color coding of fluorescence with red coding for high levels of fluorescence and blue color for low levels. Excitation = 570 nm, emission = 650 nm. (B) Representative microscope image of histochemical analysis of the tumor tissue induced with magnetic field for 4 h after i.v. administration. (H&E and Prussian Blue stain, 40×).

3.7. Antitumor efficacy

The differences of tumor inhibition rate affected by different nanocomposites and different treatment modes are shown in Table 2. In the MTX@uGO-COOH@MNP@OA@CPT treatment group, in the absence of NIR radiation, the tumor inhibition rate was 40.1%, reflecting the certain antitumor efficacy of the composite. However, when tumor-bearing mice were treated using the same composite accompanied by NIR radiation, the tumor inhibition rate could increase to 73.9%, which was the highest among four given composite therapeutic patterns. The differences are significant ($P<0.05$) as compared with the control group and group 2. Their tumor volumes were correspondingly the smallest among all groups [Fig. 9 (e)]. This result was close to that caused by cRGD-functionalized polymeric magnetic nanoparticles previously reported by us,[21] where the tumor inhibition rate was 75.6%. An important reason was that MNPs captured in nanocomposite could transform irradiation energy into heat under NIR, leading to tumor cell necrosis because of hyperthermia. In single drug-loaded MTX@uGO-COOH@MNP@OA and uGO-COOH@MNP@OA@CPT treatment groups, the tumor inhibition rate dipped to 58.5% and

61.3%, and their tumor volumes slightly larger [Fig. 9 (c, d)] than group e, respectively, although photothermal therapy was also supplied, indicating that the antitumor efficacy reduced due to the absence of collaborative treatment of dual drug. These results were similar to that caused by doxorubicin in combination with photodynamic therapy, where the tumor inhibition rate was less than 58%.[38] The therapeutic window of free CPT, free MTX and their combination was also provided in order to see if dual-drug treatment enhanced antitumor efficacy and the amount of drug released from the nanocomposites is within this critical parameter for real clinical applications. The results were presented in SI 4.

Table 2 The anticancer properties of nanocomposites combined without or with photothermal therapy in S-180 sarcoma-bearing Balb/c mice. The data are expressed as mean±S.D (n=5).

No.	Groups	NIR radiation	Tumor mass (g)	Tumor inhibitory rate (%)[a]
1	Control (PBS)	No	1.42 ± 0.31	—
2	MTX@uGO-COOH@MNP@OA@CPT	No	0.85 ± 0.27[b]	40.1 ± 4.2
3	MTX@uGO-COOH@MNP@OA@CPT	Yes	0.37 ± 0.23[b, c]	73.9 ± 4.5[c]
4	MTX@uGO-COOH@MNP@OA	Yes	0.59 ± 0.24[b]	58.5 ± 3.8
5	uGO-COOH@MNP@OA@CPT	Yes	0.55 ± 0.22[b]	61.3 ± 4.1

[a] Tumor inhibitory rate (%) were calculated on the basis of tumor mass. [b] $p < 0.05$ vs control group, [c] $p < 0.05$ vs group 2.

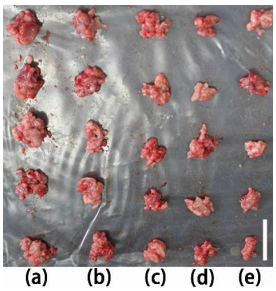

Fig. 9. Morphology of tumor tissues from sarcoma 180-bearing mice treated with various composites by tail intravenous injection on alternate days for 14 days, respectively. (a) Control group was injected 0.2 mL of sterile PBS. (b-e) The treated groups: (b) MTX@uGO-COOH@MNP@OA@CPT; (c) MTX@uGO-COOH@MNP@OA; (d) uGO-COOH@MNP@OA@CPT; (e) MTX@uGO-COOH@MNP@OA@CPT. The treated groups were injected 0.2 mL of composite suspensions at a dose of 2 mg/kg body weight combined without (b) or with (c-e) NIR radiation in each time treatment. The scale bar in figure shows 2 cm.

The in vivo antitumor efficacy of MTX@uGO-COOH@MNP@OA@CPT composite in the sarcoma 180-bearing mice model was confirmed using histopathology assay (Fig. 10). As shown in Fig. 10A, necrosis cell nuclei were hardly detectable in control group, where tumor tissue presented abundant blood vessels (V) and dense huge cell nuclei (N), suggesting that tumor cells

were in the exuberant growth period. Although the tumor tissues from MTX@uGO-COOH@MNP@OA@CPT treatment group (without NIR radiation, Fig. 10B) showed some intercellular space (S), there were huge mellow cell nuclei, indicating that the growth of tumor cells were not completely under control. The tumor tissues from MTX@uGO-COOH@MNP@OA and uGO-COOH@MNP@OA@CPT (with NIR radiation, Fig. 10C, 10D) treatment groups held nonuniform cell nuclei and atrophic blood vessels (V), reflecting that the growth of tumor cells were inhibited to a certain degree. By contrast, tumor tissues from MTX@uGO-COOH@MNP@OA@CPT treatment group accompanied by NIR radiation (Fig. 10E) have widespread holes (H) and uniform small cell nuclei. The emergence of the large area of the acellular zone means many cell necrosis, which powerfully reinforces the idea that the antitumor effect is significant using dual drug-loaded graphene oxide/Fe_3O_4 nanocomposites combined with photothermal therapy.

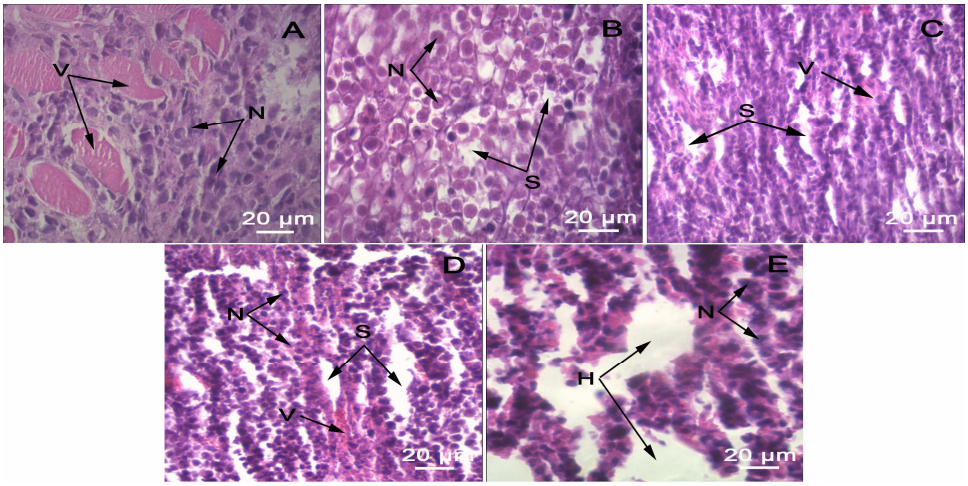

Fig. 10. Representative histopathologic images of tumor tissues from sarcoma 180-bearing mice treated with various composites by tail intravenous injection on alternate days for 14 days, respectively. (A) Control group was injected 0.2 mL of sterile PBS. (B-E) The treated groups: (B) MTX@uGO-COOH@MNP@OA@CPT; (C) MTX@uGO-COOH@MNP@OA; (D) uGO-COOH@MNP@OA@CPT; (E) MTX@uGO-COOH@MNP@OA@CPT. The treated groups were injected 0.2 mL of composite suspensions at a dose of 2 mg/kg body weight combined without (B) or with (C-E) NIR radiation in each time treatment (H&E stain, 40×).

4. Summary

In summary, the resulting uGO-COOH@MNP@OA hybrid shows superparamagnetic property with specific accumulation capacity to tumor site by the induction of an external magnetic field. Encapsulation efficiencies of CPT and MTX on the carrier significantly increased due to the

introduction of a hydrophobic OA shell on the surface of MNPs and the modification of carboxyl groups on uGO. The nanocomposite showed a pH-depended drug release pattern, in which anticancer drugs MTX and CPT could mainly be released around tumor tissues. Increased drugs and MNPs accumulation in the tumor and the consequent dual-drug synergic effect and hyperpyrexia significantly contribute to enhancement in inhibition of tumor growth and induction of necrosis.

Acknowledgment

This study was supported by the Talents Fund for Basic Disciplines of National Science Fundation of China (J. 1210077, J. 1210033, J. 1103502) and the basic scientific research business expenses of the central university and open project of key laboratory for magnetism and magnetic materials of the ministry of education, Lanzhou University (no. LZUMMM2012006).

Notes

[a] Department of Biochemistry and Molecular Biology, School of Life Sciences, Lanzhou University, Lanzhou, Gansu 730000, China

[b] Key Lab of Preclinical Study for New Drugs of Gansu Province, Lanzhou, Gansu 730000, China

[c] College of Chemistry and Chemical Engineering, Lanzhou University, Lanzhou, Gansu 730000, China

* Corresponding author, Fax: +86-931-891-5208; Tel: +86-15117266908.

E-mail: shenjianmin@lzu.edu.cn (Jianmin Shen)

References

1 Z. B. Gao, L. N. Zhang and Y. J. Sun, *J. Control. Release*, 2012, **162**,45.

2 L. H. Hurley, *Nat. Rev. Cancer*, 2002, **2**, 188.

3 Q. Yin, J. N. Shen, Z. W. Zhang, H. J. Yu and Y. P. Li, *Adv. Drug Deliver. Rev.*, 2013, DOI 10.1016/j.addr.2013.04.011.

4 D. S. Backos, C. C. Franklin and P. Reigan, *Biochem. Pharmacol.*, 2012, **83**,1005.

5 E. I. Deryugina and J. P. Quigley, *BBA-MolCell Res.*, 2010, **1803**, 103.

6 G. P. Sun and K. D. Irvine, *Dev. Biol.*, 2011, **350**,139.

7 J. K. Vasir and V. Labhasetwar, *Technol. Cancer Res. T.*, 2005, **4**,363.

8 T. Tsuruo, M. Naito, A. Tomida, N. Fujita, T. Mashima, H. Sakamoto and N. Haga, *Cancer Sci.*, 2003, **1**,15.

9 A. Galbiati, C. Tabolacci, B. M. D. Rocca, P. Mattioli, S. Beninati, G. Paradossi and A. Desideri,

Bioconjugate Chem., 2011, **22**, 1066.

10 B. Rafique, A. M. Khalid, K. Akhtar and A. Jabbar, *Biosens. Bioelectron.*, 2013, **44**, 21.

11 A. Singh, F. Dilnawaz, S. Mewar, U. Sharma, N. R. Jagannathan and S. K. Sahoo, *ACS Appl. Mater. Interfaces*, 2011, **3**, 842.

12 E. Blanco, E. A. Bey, Y. Dong, B. D. Weinberg, D. M. Sutton, D. A. Boothman and J. Gao, *J. Control. Release*, 2007, **122**, 365.

13 Y. Z. Wang, Y. Q. Zhang, B. C. Wang, Y. Cao, Q. S. Yu and T. Y. Yin, *J. Nanopart. Res.*, 2013, **15**, 1726.

14 K. Y. Win and S. S. Feng, *Biomaterials*, 2005, **26**, 2713.

15 Y. M, S. Tong, G. Bao, C. Gao and Z. F. Dai, *Biomaterials*, 2013, **34**, 7706.

16 L. Z. Bai, D. L. Zhao, Y. Xu, J. M. Zhang, Y. L. Gao, L. Y. Zhao and J. T. Tang, *Mater. Lett.*, 2012, **68**, 399.

17 M. Q. Chu, Y. X. Shao, J. L. Peng, X. Y. Dai, H. K. Li, Q. S. Wu and D. L. Shi, *Biomaterials*, 2013, **34**, 4078.

18 J. M. Shen, F. Y. Gao, T. Yin, H. X. Zhang, M. Ma, Y. J. Yang and F. Yue, *Pharmacol. Res.*, 2013, **70**, 102.

19 J. M. Shen, T. Yin, X. Z. Tian, F. Y. Gao and S. Xu, *ACS Appl. Mater. Interfaces*, 2013, **5**, 7014.

20 T. Y. Liu, S. H. Hu, K. H. Liu, R. S. Shaiu, D. M. Liu and S. Y. Chen, *Langmuir*, 2008, **24**, 13306.

21 J. M. Shen, F. Y. Gao, T. Yin, H. X. Zhang, M. Ma, Y. J. Yang and F. Yue, *Pharmacol. Res.*, 2013, **70**, 102.

22 J. M. Shen, X. M. Guan, X. Y. Liu, J. F. Lan, T. Cheng and H. X. Zhang, *Bioconjugate. Chem.*, 2012, **23**, 1010.

23 X. Y. Yang, Y. S. Wang, X. Huang, Y. F. Ma, Y. Huang, R. C. Yang, H. Q. Duan and Y. S. Chen, *J. Mater. Chem.*, 2011, **21**, 3448.

24 C. Y. Wang, S. Ravi, U. S. Garapati, M. Das, M. Howell, J. Mallela, S. Alwarappan, S. S. Mohapatrabc and S. Mohapatra, *J. Mater. Chem. B*, 2013, **1**, 4396.

25 W. H. Chen, P. W. Yi, Y. Zhang, L. M. Zhang, Z. W. Deng and Z. J. Zhang, *ACS Appl. Mater. Interfaces*, 2011, **3**, 4085.

26 H. M. Sun, L. Y. Cao and L. H. Lu, *Nano Res.*, 2011, **4**, 550.

27 P. Liu, W. Zhong, X. L. Wu and J. H. Qiu, *Chem. Eng. J.*, 2013, **219**, 10.

28 X. X. Ma, H. Q. Tao, K. Yang, L. Z. Feng, L. Cheng and X. Z. Shi, *Nano Res.*, 2012, **5**, 199.

29 X. Y. Yang, X. Y. Zhang, Y. F. Ma, Y. Huang, Y. S. Wang and Y. S. Chen, *J. Mater. Chem.*, 2009, **19**, 2710.

30 W. S. Hummers and R. E. Offeman, *J. Am. Chem. Soc.*, 1958, **80**, 1339.

31 P. F. Liu, H. Z. Wang, Y. G. Li and Y. R. Duan, J. Macromol. *Sci., Part A*, 2009, **46**, 1024.

32 J. S. Huang, S. R. Wan, M. Guo and H. S. Yan, *J. Mater. Chem.*, 2006, **16**, 4535.

33 H. Q. Bao, Y. Z. Pan, Y. Ping, N. G. Sahoo, T. F. Wu, L. Li and L. H. Gan, *Small*, 2011, **7**, 1569.

34 L. M. Zhang, J. G. Xia, Q. H. Zhao, L. W. Liu and Z. J. Zhang, *Small*, 2010, **6**, 537.

35 P. Chandna, M. Saad, Y. Wang, E. Ber, J. Khandare and A. A. Vetcher, *Mol. Pharm.*, 2007, **4**, 668.

36 K. H. Min, K. Park, Y. S.Kim, S. M. Bae, S. Lee, H. G. Jo, R. W. Park, I. S. Kim, S. Y. Jeong, K. Kim and I. C. Kwon, *J. Control. Release*, 2008, **127**, 208.

37 T. G. Burke, A. E. Staubus and A. K. Mishra, *J. Am. Chem. Soc.*, 1992, **114**, 8318.

38 A. Khdair, D. Chen, Y. Patil, L. N. Ma, Q. P. Dou, M. P. V. Shekhar and J. Panyam, *J. Control. Release*, 2010, **141**,137.